

1 **REVISION 1**

2  
3 **Melting curve minimum of barium carbonate BaCO<sub>3</sub> near 5 GPa**

4  
5 Junjie Dong<sup>1†\*</sup>, Jie Li<sup>1</sup>, Feng Zhu<sup>1‡</sup>, Zeyu Li<sup>1</sup>, Rami Farawi<sup>1</sup>

6  
7 <sup>1</sup>Department of Earth and Environmental Sciences, University of Michigan, Ann Arbor, MI 48109, USA.

8 <sup>†</sup>Now at Department of Earth and Planetary Sciences, Harvard University, Cambridge, MA 02138, USA.

9 <sup>‡</sup>Now at Hawaii Institute of Geophysics and Planetology, University of Hawai'i at M<sup>o</sup>noa, Honolulu, Hawai'i, USA

10 <sup>\*</sup>Correspondence to: Junjie Dong (E-mail: [junjiedong@g.harvard.edu](mailto:junjiedong@g.harvard.edu))

11  
12 **ABSTRACT**

13  
14 The melting point of barium carbonate (BaCO<sub>3</sub>) was determined at pressures up to 11 GPa using  
15 the ionic conductivity and platinum (Pt) sphere methods in a multi-anvil press. The melting point  
16 decreases with pressure from 2149 ± 50 K at 3 GPa to a fitted local minimum of 1849 K at 5.5  
17 GPa, and then it rises with pressure to 2453 ± 50 K at 11 GPa. The fitted melting curve of BaCO<sub>3</sub>  
18 based on the ionic conductivity measurements is consistent with the Pt sphere measurements that  
19 were carried out independently at selected pressures. The negative slope of the BaCO<sub>3</sub> melting  
20 curve between 3 and 5.5 GPa indicates that the liquid is denser than the solid within this pressure  
21 range. Synchrotron X-ray diffraction (XRD) measurements in a laser-heated diamond anvil cell  
22 (LH-DAC) showed that BaCO<sub>3</sub> transformed from the aragonite structure (*Pmcn*) to the post-  
23 aragonite structure (*Pmmn*) at 6.3 GPa and 1026 K as well as 8 GPa and 1100 K and the post-  
24 aragonite structure remained metastable upon quenching and only reverted back to the witherite  
25 structure upon pressure release. The local minimum near 5 GPa is attributed to the triple point  
26 where the melting curve of BaCO<sub>3</sub> meets a phase transition to the denser post-aragonite structure  
27 (*Pmmn*). Local minima in the melting curves of alkaline earth carbonates would lead to incipient  
28 melting of carbonated rocks in Earth's mantle.

29  
30 **Keywords:** *barium carbonate, melting point, density crossover, phase transition, negative*  
31 *melting slope, post-aragonite structure*

## 33 INTRODUCTION

34

35 Alkaline earth carbonates, primarily  $\text{CaCO}_3$  and  $\text{MgCO}_3$ , play important roles in  
36 transporting carbon into the deep mantle through subducting slabs (e.g. Dasgupta 2013). A recent  
37 study suggests a local minimum in the melting curve of  $\text{CaCO}_3$  near 13 GPa, likely resulting  
38 from a phase transition that intersects the melting curve, but the inferred negative melting slope  
39 is not clearly resolved (Li et al. 2017). Another alkaline earth carbonate,  $\text{BaCO}_3$  is shown to  
40 undergo similar pressure-induced aragonite to post-aragonite phase transition as  $\text{CaCO}_3$  but at  
41 lower pressures (Shatskiy 2015). Investigating the melting behavior of  $\text{BaCO}_3$  will allow for  
42 testing the occurrence of solid-liquid density crossover in compressed alkaline earth carbonates.  
43 Furthermore, systematic comparison of the structure and stability of alkaline earth carbonates is  
44 useful for constructing thermodynamic models to predict the melting behavior of complex  
45 mantle rocks in a petrologically-relevant pressure-temperature-composition space (Hurt and  
46 Wolf 2018).

47 The melting behavior of  $\text{BaCO}_3$  at ambient conditions is currently unresolved. The  
48 reported melting point ranges from 1084 K (<https://www.alfa.com/en/catalog/010645/>), 1653 K  
49 (National Bureau of Standards) to 1828 K (CRC Handbook of Chemistry and Physics, 98<sup>th</sup>  
50 Edition). Some studies suggest that  $\text{BaCO}_3$  decomposes in the solid state to  $\text{BaO}$  and  $\text{CO}_2$  (e.g.  
51 Arvanitidis et al. 1996). Data on the melting behavior of  $\text{BaCO}_3$  at higher pressures are not  
52 available. In this study, the melting curve of  $\text{BaCO}_3$  as well as the phase boundary between the  
53 aragonite and post-aragonite phases of  $\text{BaCO}_3$  were investigated experimentally at upper mantle  
54 conditions. The results were applied to examine the influence of solid-solid transitions on the  
55 shape of the melting curve and explore the implications for the melting behavior of carbonated  
56 rocks in Earth's mantle.

57

## 58 METHOD

59

60 Fine powder of high-purity  $\text{BaCO}_3$  (Alfa Aesar 10645, 99.997%) was used as the starting  
61 material. Prior to experiments, the sample was kept in a vacuum oven at 400 K to remove  
62 moisture.

## 63 Multi-anvil experiments

64

a)

b)

Figure 1. Experimental configuration of ionic conductivity measurements in a multi-anvil press. (a) Configuration of the modified COMPRES 5-mm cell assembly. The electrodes and the thermocouple were placed symmetrically along the rotational axis of the cell assembly for reliable measurements of melting temperature. (b) Pictorial diagram of the circuit with a type-C thermocouple and a pair of Pt electrodes.

65 Ionic conductivity experiments were performed at pressures between 3 and 11 GPa using  
66 a 1000-ton Walker-type multi-anvil press at the University of Michigan. Toshiba-Tungaloy F-  
67 grade tungsten carbide cubes with 5-mm truncation edge length (TEL) and the COMPRESS 10/5  
68 assembly (Leinenweber et al. 2012) were used to generate high pressures and high temperatures.  
69 Closed high-pressure cell assemblies were dried in a vacuum oven at 400 K for 8-24 hours  
70 before loading into the multi-anvil press. The uncertainty in pressure measurement is estimated  
71 to be  $\pm 7\%$ . This includes the precision of pressure calibration of  $\pm 5\%$  estimated on the basis of  
72 duplicate experiments, and systematic errors of  $\pm 5\%$  arising from the effect of temperature on  
73 pressure calibration and pressure drift during heating and cooling (Li and Li 2015). A standard  
74 type-C thermocouple (TC) was used to monitor temperature. The uncertainty in the measured  
75 temperature is estimated to be  $\pm 50$  K. This includes the precision in the thermocouple  
76 calibration and the position of the TC junction relative to the sample (Li and Li, 2015) but  
77 ignores the effect of pressure on the electromotive force (emf) of the TC. Limited data suggest  
78 that the type-C TC underestimates temperature and that systematic error generally increases with  
79 pressure and temperature, rising to tens of degrees at 10 GPa and above 2000 K (Li et al. 2003).  
80 As a result, the measured melting points of  $\text{BaCO}_3$  at  $> 10$  GPa may be lower than the real values

81 by a few tens of degrees.

82 The cell assembly for the ionic conductivity measurements (Fig. 1a) was modified from  
83 the COMPRESS 10/5 assembly, similar to that of Li et al. (2017). Two pairs of slots were cut at  
84 both ends of the Re furnace and the LaCrO<sub>3</sub> sleeve to fit the TC and Pt electrode wires. A pair of  
85 Pt wires were inserted into one of the four-bore Al<sub>2</sub>O<sub>3</sub> tubing and served as the electrodes. Each  
86 4-bore alumina (Al<sub>2</sub>O<sub>3</sub>) tubing was enclosed in a Pt tube, which was further surrounded by a  
87 magnesia (MgO) sleeve. The electrode tips and TC junction were placed along the rotational axis  
88 of the cylindrical-shaped heater and at the same distance to the equator of the heater, so that the  
89 TC measured the temperature at the electrode tips. Both the TC junction and electrode tips were  
90 positioned within the middle third of the heater length, where the temperature gradient is  
91 estimated to be less than 100 K (Leinenweber et al. 2012).

92 The circuit for ionic conductivity measurements (Fig. 1b) includes a Mastech variable  
93 transformer and a Fluke 289 multi-meter. External electromagnetic interference, including  
94 heating current and the pressure control motor, is less than a few #A and negligible compared  
95 with the ionic current through molten BaCO<sub>3</sub>.

96 In a typical experiment, the ionic current through the compressed sample was monitored  
97 during multiple heating and cooling cycles at a given pressure, and the same recording procedure  
98 was repeated at several pressures along its compressional path. The sample was pressurized at a  
99 rate of 1 to 3 GPa per hour to the target pressure, and then heated at a rate of 60 K per minute. In  
100 some experiments, the assembly was sintered at 1273 K for 1-2 hours, and then further heated  
101 until a current jump was detected. After heating, the sample was cooled at the rate of 180 K per  
102 minute to 1473 K, and then heated up again for more heating cycles to repeat the melting  
103 detection. At each pressure, at least two heating cycles were completed before the sample was  
104 compressed to the next target pressure. Melting measurements were repeated multiple times at  
105 different pressures in each experiment. At the highest pressure and temperature of each  
106 experiment, the sample was quenched by turning off the power.

107 To cross-validate the ionic conductivity measurements, Pt sphere experiments without  
108 electrodes were conducted independently using the same multi-anvil press. During sample  
109 loading, a Pt sphere of 100 to 200 #m in diameter was placed near the top of the sample. After  
110 heating and recovering the sample, the location of the Pt sphere was used to determine whether  
111 the sample was molten or not at the target temperature. Pt sphere experiments at 5.5 and 8 GPa

112 used the standard COMPRESS 10/5 assembly with Pt capsule, and the experiment at 1.4 GPa  
113 used cast octahedra and Fansteel tungsten carbide cubes with 8-mm TEL. At the target pressure,  
114 the sample was heated to the target temperature and held for 5 min before quenched by turning  
115 off the power. The multi-anvil press is calibrated for pressures above 2 GPa and therefore a  
116 larger pressure error may be present in the experiment at 1.4 GPa where some ceramic parts may  
117 have not be fully equilibrated under compression.

118 The experimental products were recovered and examined for texture, composition, and  
119 structure. An optical microscope was used to check the position of the electrode tips and  
120 thermocouple junctions and locate the Pt sphere in the sample. Raman spectra were collected on  
121 a Renishaw Raman microscope for phase identification. Back-scattered-electron (BSE) images  
122 and energy dispersive spectra (EDS) were obtained on a JOEL 7800 FLV field emission SEM in  
123 the Central Campus Electron Micro-beam Analysis Laboratory (EMAL) at the University of  
124 Michigan. The BSE and EDS results were inspected to make sure that products were free of  
125 contamination from the four-bore Al<sub>2</sub>O<sub>3</sub>, the Pt parts or other components in the assembly, which  
126 were in direct contact with the sample or might diffuse into the sample.

127

### 128 **Diamond anvil cell experiments**

129 Synchrotron XRD measurements were conducted to investigate the phase stability of  
130 BaCO<sub>3</sub> at high pressures and high temperatures using a laser-heated diamond anvil cell. A  
131 symmetric cell with 400-#m culet diamond anvils was used to generate high pressures. A Re  
132 gasket was pre-indented to ~35 #m thickness and drilled to form a sample chamber with 200 #m  
133 diameter. Fine powders of BaCO<sub>3</sub> were mixed with about 5 wt% Pt powder and dried in vacuum  
134 oven at 400 K overnight before loading into the DAC. The Pt powder was used as a laser  
135 absorber and secondary pressure standard. Two ~10 #m Ruby spheres were loaded as the  
136 primary pressure standard. The sample was immersed in neon as the pressure transmitting  
137 medium and thermal insulator.

138 Laser heating and angular dispersive XRD measurements were conducted at the  
139 Advanced Photon Source (APS), Beamline 16-ID-B of HPCAT. The sample was heated from  
140 both sides by two identical Nd:YLF lasers ( $\lambda = 1053$  nm) with 30-micron laser spots.  
141 Temperatures were determined by fitting thermal radiation spectrum to the gray body radiation

#6891 Revision 1 to *American Mineralogist*

142 function (Meng et al. 2015). For a 30-second acquisition time, the temperature measurements  
 143 yielded readings of 1000-1200K. The acquisition time was reduced to 15 s at temperatures above

! "#\$%&' ! "#=GA >=B@, ?%NDBH@A@DBE%, BH%G=EF?@E%DM%N@DBAN%  
 NDBHFN@AJ@K%=" "#=GA >=B@E

! "#\$%&'	( )%* + ( , -	. /%* 0-
R3 : 2768	1\$1	2341
	5\$6	2327
	8\$3	6957
	: \$3	6946
	9\$3	2253
	63\$3 <sup>;</sup>	2151
	66\$3 <sup>;</sup>	2581
R353 : 64	1\$1	237 :
	5\$3	6974
	8\$3	6741
	4\$3	6911
	: \$3	2371
R3 : 2 : 6 :	1\$3	2659
	4\$3	6751
R37316 :	8\$8	6948
	4\$8	2323
	7\$3	269 :
R37346 :	: \$3	6946
	7\$3	2657
	9\$3	2281
	63\$3 <sup>;</sup>	2147

)% (G=EEFG=%FBN=G@, AB@K%AE%O% : % P \$  
 /% . =>#=G, @FG=E%, G=%, J=G, C=E%DM% >=?@ABC%#DAB@E%  
 >=, EFG=>=B@E%MGD>%, @%?=, E@%QD%<=, @ABC%NKN?=@E%, BH%  
 FBN=G@, AB@K%AE%O%83%O\$  
 :% . <=%>=?@ABC%#DAB@E%>=, EFG=H%, IDJ=%63%+ ( , %>, K%  
 <, J=%?, GC=%=GGDGE%HF=%@D%@<=%?AL?=%K%>=?@ABC%DM% ( @S

**Table 2** Results of Pt sphere experiments

Exp. ID	P (GPa)	T (K)	Result
M110917	1.4	2073	not sink
M112117	5.5	2011	sink
M120117	5.5	2023	sink
M123117	8.0	2223	sink

144 1200 K. The temperature of the heated samples was measured with an accuracy of ± 100 K  
 145 (Errandonea et al. 2003). The X-ray beam was monochromatized to a wavelength of 0.4066 Å  
 146 and focused to an area of 5.3 μm × 4.4 μm. Diffraction images were recorded for 15 s with a  
 147 MAR CCD detector.

148 Synchrotron XRD patterns of BaCO<sub>3</sub> were recorded at temperatures up to 1500 K and at  
149 pressures up to 30 GPa. At several pressure points near the phase boundary, the sample was

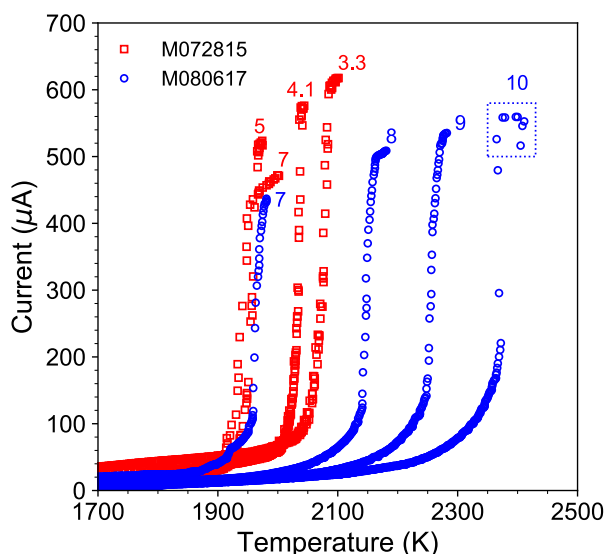


Figure 2. Representative current-temperature measurements during heating cycles at high pressures. M072815 (red squares) and M080617 (blue circles). The melting point is located by the maximum of the first derivative of the current ( $dI/dT$ ). The dashed rectangle (blue) shows fluctuation in the current after melting at 10 GPa, indicating melting of the Pt capsule or electrodes.

150 laser-heated at a small power step until a temperature reading could be obtained. A series of  
151 XRD patterns of the heated spot were recorded at different temperatures and after quenching to  
152 300 K. The 2-D images were integrated into 1-D patterns using Dioptas (Prescher and  
153 Prakapenka, 2015) and refined using the PDIndexer software (Seto et al. 2010).

154

## 155 RESULTS AND DISCUSSION

### 156 Melting points of BaCO<sub>3</sub> from ionic conductivity and Pt sphere experiments

157 The melting points of BaCO<sub>3</sub> between 3 and 11 GPa were determined in five ionic  
158 conductivity experiments (Table 1). At a given pressure, melting was detected on the basis of a  
159 steep rise in the ionic current through the sample (Fig. 2 and Supplementary Data). Upon  
160 heating, the current through the samples remained at a fairly low value of a few to a few tens of  
161 microamps before soaring to several hundred microamps near the melting point. Further heating  
162 led to a plateau or smaller rise in current. The current-temperature relation reversed upon  
163 cooling, with a steep decrease usually 50 to 100 K lower than the melting point detected during  
164 heating. The rise and fall of sample current were repeatedly measured over multiple heating and  
165 cooling cycles at a given pressure. The rapid rise in ionic current is attributed to the dissociation  
166 of crystalline ionic bonding, which is endothermic and reversible. The hysteresis can be  
167 explained by supercooling due to kinetic barrier in nucleation (Gali&ski et al. 2006), which exists

168 for freezing but not melting, hence we located the melting points based on the steep current rise  
169 in the heating cycles.

170 As reported previously (Li et al. 2017), pre-melting rise in ionic conductivities introduces

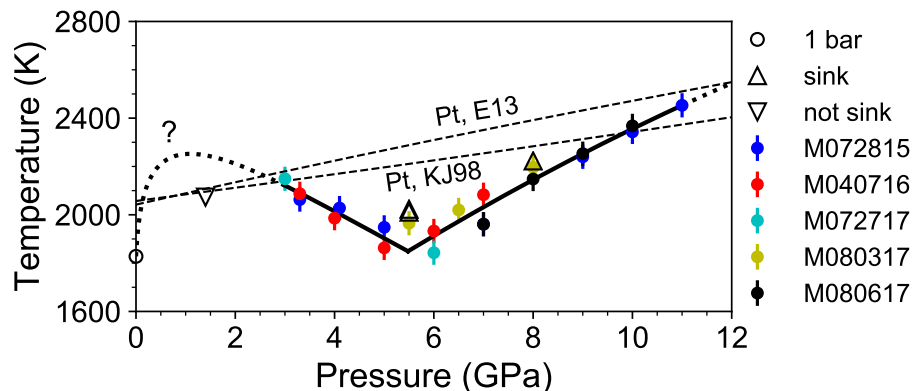


Figure 3. Melting curve of BaCO<sub>3</sub> at high pressures. The melting curve is established from the ionic conductivity measurements in Table 1 (filled circle with error bar), by fitting the melting points from 1 bar to 5 GPa to a Kechin melting equation (Kechin, 2001) and a second-order polynomial from 5.5 to 11 GPa. The melting curve between 1 bar and 3 GPa (dotted line) is back-extrapolated from the Kechin melting curve (Eq.1) but has not been confirmed experimentally. A melting minimum is located near 5.5 GPa and 1849 K, where the two segments of the fitted melting curve cross. Results of Pt sphere experiments (triangle down: not sink; triangle up: sink) are plotted for cross-validation. The melting curves of Pt (dashed lines, Errandonea 2013 and Kavner and Jeanloz 1998) cross the fitting melting curve of BaCO<sub>3</sub> multiple times, near 1 bar, 3 GPa, and 10-12 GPa.

171 uncertainties in locating the melting point (Fig. 2). The current starts to increase at 50 to 100 K  
172 below the melting point and ramps up at an increasing rate towards melting, likely due to crystal  
173 defects created at high temperatures (Hayes and Hutchings 1989). Different criteria may be  
174 adopted to place the onset of melting at the beginning, middle, or end of the steep rise. For  
175 consistency, the middle point of the steepest segment of the current-temperature curve, where  
176  $dI/dT$  reached the maximum value, was taken as the melting point. The melting points measured  
177 in multiple heating cycles at a given pressure typically differ by less than 20 K and the average  
178 values are reported (Table 1). Among different experiments the measured melting temperature at  
179 a given pressure agree to within 100 K.

180 In an attempt to measure the melting point of BaCO<sub>3</sub> at 1 bar, we heated BaCO<sub>3</sub> in a Pt  
181 crucible to 1173 K using an electric furnace at the rate of 60 K per minute, and then cooled it in  
182 air to room temperature. The sample was then weighed using a Mettler-Toledo balance and  
183 examined under a Leica microscope for mass and textural change. Its weight loss clearly  
184 indicated decomposition, possibly in combination with melting. The Alfa Aesar value of 1084 K



185 is similar to the witherite-trigonal phase transition at ~1093 K and 1 bar (Antao and Hassan  
186 2007), or it may correspond to the eutectic melting between BaCO<sub>3</sub> and BaO at a specific partial  
187 pressure of CO<sub>2</sub>. A furnace with controlled CO<sub>2</sub> partial pressure is required to determine the  
188 melting and decomposition behavior of BaCO<sub>3</sub>. Here we take the CRC value at 1828 K as the  
189 nominal melting point of BaCO<sub>3</sub> at 1 bar.

190 Melting point data from 1 bar to 5 GPa were used to fit a Kechin melting equation  
191 (Kechin, 2001) (Eq. 1):

192

$$193 \quad T_m = T_0 + \frac{a}{P - P_0} + b(P - P_0)^c + d(P - P_0)^e \quad (1)$$

194

195 and melting data above 5.5 GPa were fitted to a second order polynomial (Eq. 2) from 5.5 to 11  
196 GPa:

197

$$198 \quad T_m = a + bP + cP^2 + dP^3 + eP^4 \quad (2)$$

199

200 where T<sub>m</sub> and T<sub>0</sub> are the melting point and the reference temperature in K, and P and P<sub>0</sub> are the  
201 pressure and the reference pressure in GPa. Here, the reference condition is the melting point of  
202 BaCO<sub>3</sub> at 1 bar, T<sub>0</sub> = 1828 K and P<sub>0</sub> = 1 bar ~ 0 GPa. Fitted melting curve parameters are a =  
203 0.0382017, b = 11.6106, c = 0.0760715 and p = -2.684, q = 153.6, w = 1088.

204 Bounds on the melting point were obtained from four Pt sphere experiments at 1.4,  
205 5.5, and 8 GPa (Table 2). In M120117 and M123117, Pt spheres sank and indicated melting  
206 below 2023 K at 5.5 GPa, and below 2223 K at 8 GPa. Experiment M112117 at 5.5 GPa was  
207 quenched at 2011 K due to the failure of the heating controller. The Pt sphere also sank in this  
208 experiment, suggesting that the melting point at 5.5 GPa is likely lower than 2011 K. In  
209 M110917, the Pt sphere remained at the top of the sample, indicating that the melting point at 1.4  
210 GPa is above 2073 K. Although more Pt sphere experiments are required to bracket the melting  
211 curve independently, the bounds from the existing Pt sphere experiments are broadly consistent  
212 with the results of ionic conductivity measurements within experimental uncertainties and  
213 support the adopted criterion for locating the melting point from the current jumps (Fig 3).

214 All the recovered samples were confirmed to be BaCO<sub>3</sub> and the atomic ratio of Ba:C:O is  
215 approximately 1:1:3. EDS analyses as well as the texture of the recovered sample showed no

216 sign of chemical contamination and BaCO<sub>3</sub> did not decompose or undergo incongruent melting.  
217 In several conductivity experiments, the current reading became unstable when the temperature  
218 approached the melting point of the Pt electrode. At 10 GPa in experiment M080617, the current  
219 dropped noticeably after the melting temperature was reached (Fig. 2). At this pressure the  
220 melting point of BaCO<sub>3</sub> may be still 120 K below that of Pt (Errandonea 2013) or have exceeded  
221 the Pt melting temperature (Kavner and Jeanloz 1998). Likewise, the measured melting point of  
222 BaCO<sub>3</sub> at 3 GPa falls between the two reported Pt melting points at 2180 K (Errandonea 2013)  
223 and 2137 K (Kavner and Jeanloz 1998). No sample was recovered from these experiments  
224 because the Pt capsules melted. The crossing between the melting curves of BaCO<sub>3</sub> and Pt limits  
225 the application of this experimental configuration at pressures below 3 GPa and above 10-12  
226 GPa (Fig. 3).

227

### 228 **Phase boundary between aragonite and post-aragonite**

229         Synchrotron XRD measurements (Table 3) revealed the phase transformation of BaCO<sub>3</sub>  
230 from the aragonite structure (*Pmcn*) to the post-aragonite structure (*Pmmn*) at high pressures  
231 and/or high temperatures. The post-aragonite phase can be readily recognized by two distinct  
232 peaks at 6.36° and 6.70° in the XRD pattern (Fig. 4). Upon compression at 300 K, the phase  
233 transformation took place at a pressure between 8 and 9.5 GPa and room temperature. Upon  
234 heating to 1026 K at 6.3 GPa, the sample transformed fully to the post-aragonite phase. At 8.1  
235 GPa, the transformation was already complete at 1000 K. The post-aragonite phase remained  
236 metastable when the sample was cooled to 1000 K at 6.3 GPa. It was also a metastable phase  
237 when the sample was quenched to room temperature at both pressures. Upon decompression to  
238 ambient pressure, the post-aragonite phase transformed back to witherite. Our results are  
239 consistent with the results from the literatures that BaCO<sub>3</sub> transforms from aragonite to post-  
240 aragonite structure at 7-10 GPa and room temperature (Ono 2007; Ono et al. 2008; Zaoui and  
241 Sharour 2010; Townsend et al. 2013; Wang et al. 2015). Although we could not measure  
242 temperatures below 1000 K to determine the transition temperature below 9 GPa, our data  
243 suggest that the boundary between the aragonite and post-aragonite phases of BaCO<sub>3</sub> likely has a  
244 negative slope (Fig. 5). The possibility of a positive boundary (Shatskiy et al. 2015), however,  
245 cannot be ruled out because the transition may have been kinetically hindered at low  
246 temperatures.

! "#\$%&'(E) ** - #+ ( ) " ' #*# "\$+ / F+G) H I 6+)*B;DB+ ("\$\$%#\$+)AC+*# ' (#")*%#\$	! "#\$%&'(E) ** - #+ ( ) " ' #*# "\$+ / F+G) H I 6+)*B;DB+ ("\$\$%#\$+)AC+*# ' (#")*%#\$	! "#\$%&'(E) ** - #+ ( ) " ' #*# "\$+ / F+G) H I 6+)*B;DB+ ("\$\$%#\$+)AC+*# ' (#")*%#\$	! "#\$%&'(E) ** - #+ ( ) " ' #*# "\$+ / F+G) H I 6+)*B;DB+ ("\$\$%#\$+)AC+*# ' (#")*%#\$	! "#\$%&'(E) ** - #+ ( ) " ' #*# "\$+ / F+G) H I 6+)*B;DB+ ("\$\$%#\$+)AC+*# ' (#")*%#\$	! "#\$%&'(E) ** - #+ ( ) " ' #*# "\$+ / F+G) H I 6+)*B;DB+ ("\$\$%#\$+)AC+*# ' (#")*%#\$	! "#\$%&'(E) ** - #+ ( ) " ' #*# "\$+ / F+G) H I 6+)*B;DB+ ("\$\$%#\$+)AC+*# ' (#")*%#\$
12!)3	143	2"/%(	+153	+153	+153	+15 <sup>6</sup> 3
786	699	%&\$'	:8;<61=93	>8: ?>1=93	:8>9;1<3	=?>8;1<3
786	=9?7	%&&'	>89<91>3	>8: :1>3	:8>6?1:3	=?>861:3
<89	699	%&\$'	:8;6=1?3	>86; ;1?3	:8>?9163	=?9861?3
<89	==99	%&&'	:8; ;71=3	>8: =>1=3	:8>?;1=3	=?>8>1=3
;86	699	%&&'	:8; =:1<3	>86<=1=93	:8>?61=<3	==;871==3

247 The average thermal expansion coefficient of BaCO<sub>3</sub> in the post-aragonite structure is  
 248 estimated to be 3.9(8)'10<sup>-5</sup> K<sup>-1</sup> between room temperature and 1026 K at 6.3 GPa and 2.3(2)'10<sup>-5</sup>  
 249 K<sup>-1</sup> between room temperature and 1100 K at 8 GPa (Table 3). These preliminary values are  
 250 comparable to that of CaCO<sub>3</sub> (Wu et al. 1995) and MgCO<sub>3</sub> (Litasov et al. 2008) but can be better  
 251 constrained by additional synchrotron XRD experiments.

252

### 253 Melting curve minimum and solid-solid phase transition to post-aragonite structure

254 Between 3 and 11 GPa, BaCO<sub>3</sub> melted over a large range of temperatures up to 2453 K,  
 255 with a fitted melting curve minimum at 1849 K at 5.5 GPa (Fig. 3). On the low-pressure side of  
 256 the minimum, the melting temperatures of BaCO<sub>3</sub> decreases continuously from 2149 K at 3 GPa  
 257 to 1849 K at 5.5 GPa. On the high-pressure side, it increases from 1849 K at 5.5 GPa to 2453 K  
 258 at 11 GPa. The fitted melting curve decreases at a rate of ~-125 K/GPa from 3 GPa, and after  
 259 reaching the local minimum near 5 GPa, the melting curve increases at a rate of ~110 K/GPa to  
 260 11 GPa. The intersection of the fitted melting curves was determined as the local minimum at  
 261 1849 K, 5.5 GPa, where the sign of the melting slope flips from negative to positive (Fig. 5).

262 The local minimum is a prominent feature in the melting curve of BaCO<sub>3</sub>. According to  
 263 the Claudius-Clapeyron equation  $dT/dP = (V/(S = T(V/(H$ , the slope of the melting curve is  
 264 governed by the volume of fusion ( $V = V_{\text{liquid}} - V_{\text{solid}}$ ) and the entropy of fusion ( $(S = S_{\text{liquid}} -$   
 265  $S_{\text{solid}}$ ). Melting of a single component is usually an endothermic process with positive ( $H$  and  $(S$ ,  
 266 hence the sign of the melting slope is determined by the  $(V$  term: A positive sign implies that the  
 267 solid is denser than the liquid, and vice versa. A sign change indicates a density crossover  
 268 between the liquid and solid. In BaCO<sub>3</sub>, the flip of the melting slope from negative to positive  
 269 near 5 GPa indicates a density jump (volume collapse) in the solid phase.

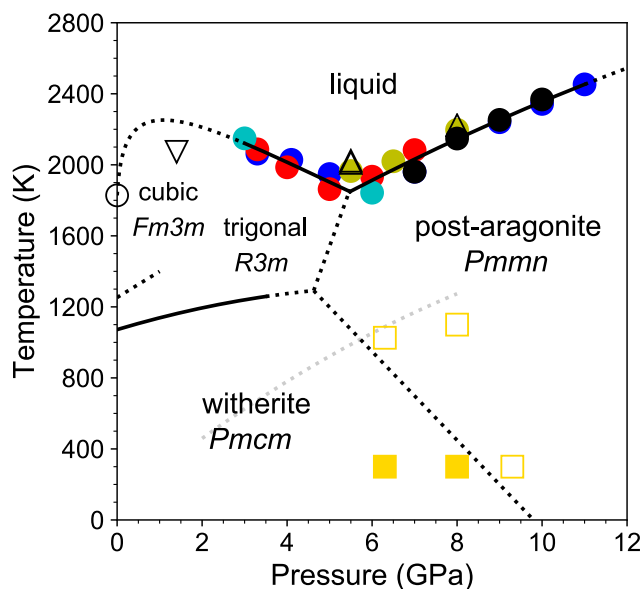


Figure 5. Phase diagram of BaCO<sub>3</sub>. The boundary between the witherite and post-aragonite BaCO<sub>3</sub> (dotted negative slope in black) is drawn according to the synchrotron XRD measurements in Table 3 (open square: post-aragonite BaCO<sub>3</sub>; filled square: aragonite BaCO<sub>3</sub>). The dotted positive slope in gray is the same phase boundary proposed in Shatskiy et al. 2015. The phase transition from witherite to trigonal BaCO<sub>3</sub> (solid, Rapoport 1967) intersects with this proposed witherite-post-aragonite boundary near 5 GPa and 1200 K. Cubic BaCO<sub>3</sub> forms at 1 bar and high temperatures and its stability field at high pressures is not known.

270 We propose that a trigonal to post-aragonite phase transition is responsible for the density  
271 crossover between the solid and liquid near 5.4 GPa. The structures of solid phases along the  
272 low-pressure segment of melting curve are not known. At least three solid polymorphs of BaCO<sub>3</sub>  
273 occur at pressures up to 6 GPa, including witherite in the aragonite structure, a trigonal calcite  
274 structure and a cubic structure (Fig. 5). Upon heating at the ambient pressure, aragonite BaCO<sub>3</sub>  
275 transforms to the trigonal structure at 1084 K (Antao and Hassan 2007), and then to a cubic  
276 structure at 1249 K (Lander, 1949; Antao and Hassan 2007; Nie et al. 2017). No further phase  
277 change has been observed up to 1573 K at ambient pressure. Studies at pressures up to 3.6 GPa  
278 found a slightly positive phase boundary between the aragonite and the trigonal phase (Rapoport  
279 and Pistorius, 1967). The cubic BaCO<sub>3</sub> has not been studied at high pressures and its stability  
280 field remains unconstrained. The transition to the cubic structure at 1249 K is thought to be  
281 driven by increased rotational activity of the CO<sub>3</sub><sup>2-</sup> groups (Lander 1949). Because the rotation  
282 is more restricted under compression, the cubic structure may become thermodynamically less  
283 favored at elevated pressures. For these reasons, we postulate that the trigonal phase is likely the  
284 high temperature BaCO<sub>3</sub> polymorph on the melting curve just below 5.5 GPa. On the high-  
285 pressure side of the melting curve minimum, the BaCO<sub>3</sub> polymorph below the melting curve is  
286 not fully resolved but the post-aragonite structure has been shown to be stable at high  
287 temperature over a broad range of pressures (e.g. Townsend et al. 2013). Assuming the post-  
288 aragonite BaCO<sub>3</sub> is the only stable phase on the high-pressure side of the melting curve

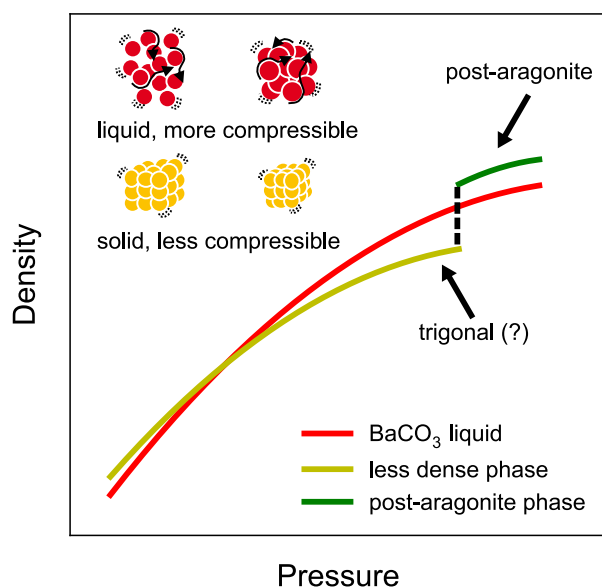


Figure 6. Schematic density profiles of liquid  $\text{BaCO}_3$ , post-aragonite  $\text{BaCO}_3$  and a less dense  $\text{BaCO}_3$  phase, likely the trigonal phase, at a constant temperature. On the high-pressure side, the phase transformation from aragonite  $\text{BaCO}_3$  (witherite) to post-aragonite  $\text{BaCO}_3$  causes an abrupt density change in the solid. The post-aragonite  $\text{BaCO}_3$  becomes denser than liquid  $\text{BaCO}_3$  above 5.5 GPa whereas the compressed liquid  $\text{BaCO}_3$  is denser than the solid from 3 to 5.5 GPa (solid line), which explains the melting curve minimum near 5 GPa. On the low-pressure side, the compressed liquid is less dense than the solid (dashed line), which explains the inferred melting curve maximum.

289 minimum, the aragonite-trigonal boundary intersects with the negative phase boundary between  
290 the aragonite and post-aragonite at a triple point near 5 GPa and 1200 K, suggesting the presence  
291 of a boundary between trigonal and post-aragonite, which is defined by the triple point and the  
292 melting curve minimum. This boundary implies that the melting curve minimum may correspond  
293 to a triple point where liquid, trigonal and post-aragonite phase of  $\text{BaCO}_3$  coexist (Fig. 5).

294 The coordination number of Ba is 6 in the trigonal structure and 12 in the post-aragonite  
295 structure (Ono et al. 2008). The difference in the coordination of Ba would make the post-  
296 aragonite phase denser than the trigonal phase and could explain the density jump at the melting  
297 minimum near 5 GPa (Fig. 6). Current knowledge of solid-solid phase transformations of  $\text{BaCO}_3$   
298 is insufficient to map out the phase diagram and therefore the melting curve minimum may be  
299 associated with other solid-solid phase transitions involving different coordination number of Ba.  
300 In addition, several metastable phases of  $\text{BaCO}_3$  were observed experimentally. A  $P2_122$   
301 rhombohedral phase was also recovered from the experiment at 15 GPa and 1273 K (Lin and  
302 Liu, 1997), while a phase transition to the trigonal phase ( $P31c$ ) was observed at 7.2 GPa and  
303 room temperature (Holl et al. 2000; Chaney et al. 2015).

304

### 305 **Melting curve maximum and possible change in liquid structure**

306 The presence of a melting curve maximum in  $\text{BaCO}_3$  is suggested by our experimental

307 data and existing constraints on the melting point at 1 bar. According to the 98<sup>th</sup> edition of the  
308 CRC Handbooks of Chemistry and Physics, the melting point at 1 bar is 1828 K, whereas Alfa  
309 Aesar Materials Safety Data Sheet listed 1084 K as the melting point, which is most likely the  
310 boundary between the aragonite and trigonal phase. Some studies found that BaCO<sub>3</sub> started  
311 decomposing at 1200 K to produce BaO and CO<sub>2</sub> vapors (L'vov and Novichikhin 1997) and  
312 decomposition proceeds in a melt after 1300 K (Galwey and Brown, 1999). The prevailing CO<sub>2</sub>  
313 pressure is known to influence its melting behavior (Judd and Pope 1972). Despite the  
314 uncertainties, the melting point of BaCO<sub>3</sub> at ambient pressure is likely equal to or less than 1828  
315 K. Our Pt sphere experiment indicates that the melting point at 1.4 GPa is above 2073 K, and  
316 therefore the melting curve has a positive slope at elevated pressures near 1 bar. Between 3 GPa  
317 and 5.4 GPa, a negative melting slope determined by our conductivity measurements implies that  
318 a local maximum of the melting curve occurs between 1 bar and 3 GPa.

319 The local maximum implies another density crossover between solid and liquid, which  
320 can be attributed to continuous changes in the liquid structure. Without long-range orders, the  
321 liquid structure is more flexible and may allow the coexistence of multiple coordination numbers  
322 (Ghiorso 2004; Stixrude and Karki 2005) and polyhedra configurations (Liu et al. 2007). As  
323 pressure increases, the average coordination number of BaCO<sub>3</sub> in the liquid may increase  
324 continuously whereas the solid phase has a fixed coordination number until a pressure-induced,  
325 discontinuous phase transition takes place. As a result, the liquid would be more compressible  
326 than the solid and have a density equals to that of the solid at the melting point maximum. If the  
327 density crossover arises from the more compressible liquid, the volume difference between the  
328 solid and liquid would increase continuously away from the local maximum, and therefore the  
329 slopes of the melting curves are expected to flatten gradually near the turning point.  
330 However, the occurrence of liquid structure change in BaCO<sub>3</sub> need to be further confirmed by  
331 future theoretical and/or experimental investigation and this particular hypothesis remain highly  
332 speculative.

333

### 334 **Systematic comparison of alkaline earth carbonates**

335 The shape of the melting curve of BaCO<sub>3</sub> resembles that of CaCO<sub>3</sub> but the melting curve  
336 minimum is more pronounced and occurs at lower pressure (Fig. 7a). In CaCO<sub>3</sub>, a local  
337 maximum was observed near 8 GPa and a local minimum occurs near 13 GPa. The negative

#6891 Revision 1 to *American Mineralogist*

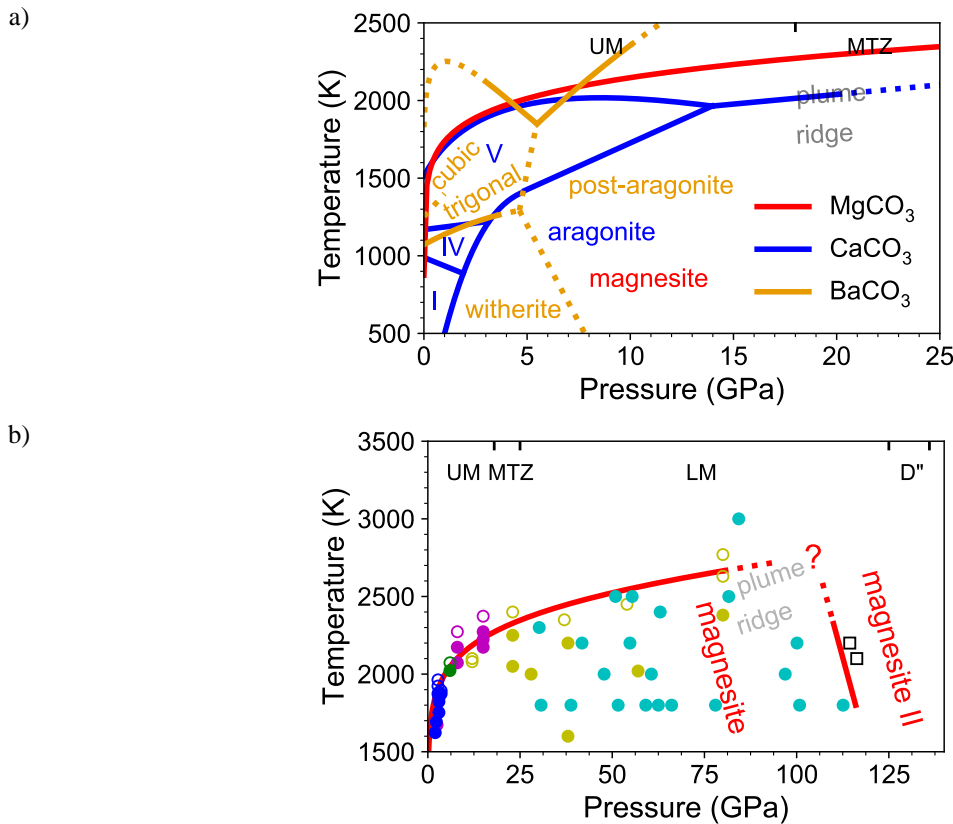


Figure 7. Systematic comparison of melting behavior of alkaline earth carbonates. a) The melting curves of  $\text{CaCO}_3$  (Li et al. 2017) and  $\text{BaCO}_3$  (this study) do not increase monotonically but have local minima, which significantly decrease melting point at high pressures and affect the order of melting of alkaline earth carbonates. Phase relations of  $\text{CaCO}_3$  are based on Li et al. 2017 and Bayarjargal et al. 2018. b) No local minimum has been observed in  $\text{MgCO}_3$ , however, a similar melting curve minimum may exist in  $\text{MgCO}_3$  resulting from the predicted phase transformation to the magnesite II phase (black open square) at megabar pressures (Isshiki et al. 2003) and possibly generate carbonate melt near core-mantle boundary or even in the lower mantle. The melting curve of  $\text{MgCO}_3$  (red) is a preliminary fit of the existing data to the Kechin melting equation ( $a = 0.0005086$ ,  $b = 11.06$ ,  $c = -0.0003971$ ,  $T_0 = 875$  K and  $P_0 = 1$  bar). Experimental data on  $\text{MgCO}_3$  were compiled from the literatures: blue for Irving and Wyllie 1973, magenta for Katsura and Ito 1990, cyan for Isshiki et al. 2003, yellow for Solopova et al. 2015 and green for Müller et al. 2017 (open circle: liquid  $\text{MgCO}_3$ ; filled circle: solid  $\text{MgCO}_3$ ). Mantle adiabat were estimated based on Herzberg et al. 2007 and Putirka et al. 2007 with a constant slope of  $dT/dP = 8$  K/GPa).

338 melting slope in  $\text{CaCO}_3$  between 8 and 13 GPa is indicated by melting points collected at  
339 multiple pressures in individual conductivity experiment, but the sign of the slope cannot be  
340 resolved when data from different experiments are combined (Li et al. 2017). The negative slope  
341 of  $\text{BaCO}_3$  from 3 to 5 GPa and the positive slope at pressures above 6 GPa are both steep and  
342 have been clearly observed experimentally. In contrast, limited data suggest that the melting  
343 point of  $\text{MgCO}_3$  increases monotonically up to 15 GPa (Irving and Wyllie 1973; Katsura and Ito

344 1990; Müller et al. 2017) and tends to flatten at higher pressures up to 80 GPa (Solopova et al.  
345 2014).

346 The occurrence or absence of the solid-solid phase transitions below the melting curve in  
347  $\text{MgCO}_3$ ,  $\text{CaCO}_3$ , and  $\text{BaCO}_3$  follow the expected inverse relation between the pressure of  
348 structure transformation (Prewitt and Downs 1998; Redfern 2000) and ionic radius ( $\text{Ba}^{2+} > \text{Ca}^{2+}$   
349  $> \text{Mg}^{2+}$ ). At the ambient temperature,  $\text{BaCO}_3$  (witherite) undergoes the aragonite to post-  
350 aragonite phase transition at 9 GPa and the same transition occurs at much higher pressure of  
351 near 40 GPa for  $\text{CaCO}_3$ , whereas the trigonal phase of  $\text{MgCO}_3$  (magnesite) remains stable up to  
352 80 GPa (Fiquet et al. 2002; Isshiki et al. 2003). The melting minimum in  $\text{CaCO}_3$  at 13 GPa is  
353 attributed to a transition from 6-coordinated calcite V to 9-coordinated aragonite phase (Fig. 7a),  
354 whereas that in  $\text{BaCO}_3$  near 5 GPa likely results from a trigonal to post-aragonite transition. The  
355 lack of a melting curve minimum in  $\text{MgCO}_3$  up to 80 GPa is consistent with the stability of the  
356 trigonal phase (Fiquet et al. 2002; Isshiki et al. 2003).

357 Although the systematics of the solid structures of alkaline earth carbonates is consistent  
358 at moderate pressures, the formation of tetrahedrally-coordinated carbon at high-pressures  
359 indicates a deviation from the systematic behavior at megabar pressures (Boulard et al. 2015).  
360 Synchrotron XRD measurements (Townsend et al. 2013) and *ab initio* calculations (Arapan  
361 2007) showed that that the post-aragonite structure of  $\text{BaCO}_3$  remained the thermodynamically  
362 favored phase up to at least 300 GPa. The phase transformation to the pyroxene-type ( $C222_1$ )  
363  $\text{BaCO}_3$  was predicted to occur at 76 GPa (Zaoui and Shahrour 2010), whereas it was not  
364 observed experimentally at the pressure of at least 150 GPa (Townsend et al. 2013). This  
365 observation seems to violate the expected systematic trend that isostructural compounds exhibit  
366 the same type of pressure-induced phase transformation and that the transition pressure is lower  
367 for larger cation (Prewitt and Downs 1998).

368

## 369 **IMPLICATIONS**

370

371 In this study, we found that the melting curve of  $\text{BaCO}_3$  involves a local minimum near 5  
372 GPa and may contain a local maximum between ambient pressure and 3 GPa. Density crossovers  
373 at the turning points are attributed to structural changes of the relevant phases along the melting  
374 curve, including solid-solid transition with abrupt change in the coordination number of divalent



375 cation and/or gradual increase in the average coordination number in the liquid. The  
376 experimentally-observed melting curve minima in both  $\text{CaCO}_3$  and  $\text{BaCO}_3$  imply that the solid-  
377 state transitions in other alkaline earth carbonate may be used to predict the occurrence of  
378 turning points in their melting curves. Given the systematic similarity of phase transformation in  
379 compressed carbonates, a minimum may occur in  $\text{MgCO}_3$  at the megabar pressure range where  
380 its melting curve intersects the phase transition from magnesite to magnesite II (Fig. 7b).

381 Accordingly, we may expect a melting curve maximum in  $\text{MgCO}_3$  resulting from the  
382 predicted transition from trigonal phase to a denser polymorph with higher coordination number  
383 at megabar pressures (Shatiskiy et al. 2015; Ishikii et al. 2003) if the comparative crystal  
384 chemistry rules still hold (Hazen et al. 2000). Previous studies suggest that the decomposition  
385 boundary of magnesite contains a minimum near 115 GPa (Ishikii et al. 2003). It is conceivable  
386 that a similar minimum exists in the melting curve of  $\text{MgCO}_3$ .

387 The occurrence of melting curve minima at different pressures implies that the order of  
388 alkaline-earth carbonate melting points changes with pressure.  $\text{BaCO}_3$  is less refractory than  
389  $\text{MgCO}_3$  and  $\text{CaCO}_3$  near 5.5 GPa but more refractory at other pressures (Fig. 7). The melting  
390 curve minima of various carbonates set the upper bound on the solidi of melting in multi-  
391 component carbonated rocks. It also dictates the composition of the incipient melt. Therefore, the  
392 solidus of a carbonated rock may have variable slopes and its composition may change  
393 considerably with pressure.

394 Discontinuous change in the slope of the melting curve is a general feature of silicate and  
395 alkaline earth carbonates, and therefore melting curves cannot be extrapolated beyond the  
396 measurement range without considering adjacent solid-solid transitions. The empirical Simon  
397 equation has been widely used to fit high-pressure melting curves (e.g., Li and Li 2015). This  
398 melting equation has the distinct advantage of not requiring any knowledge of the solid's  
399 equation of state and works well for interpolation. For a negative segment of melting curve,  
400 however, empirical Simon equation must be modified to describe the negative pressure  
401 dependence of melting temperature (Kechin 2001). Lindemann's law provides a semi-empirical  
402 scaling relation to fit discrete measurements of melting temperatures for interpolation, and in the  
403 absence of data it is often used with an equation of state to predict melting temperatures at high  
404 pressures (e.g., Li and Li 2015). Because Lindemann's law does not consider the liquid behavior,  
405 it is inadequate to represent flat or negative melting slope associated with structural changes in

406 the liquid.

407 Constraints on the melting curves shed light on the adjacent high-temperature solid  
408 polymorphs. For BaCO<sub>3</sub> the melting curve minimum is interpreted as a triple point among liquid,  
409 trigonal, and post-aragonite phases. The inferred boundary between the trigonal and post-  
410 aragonite phases need to be mapped out by measurements. Furthermore, the boundary between  
411 aragonite and post-aragonite may be narrowed down through XRD or Raman measurements  
412 using externally heated diamond anvil cells, where temperatures between room temperature and  
413 1500 K can be more precisely controlled and reliably measured to allow evaluation of kinetic  
414 effects and reversal of phase transitions.

415 Knowledge of the melting curves can also be used to establish the equation-of-state of  
416 carbonate melts and help construct thermodynamic models to predict the behavior of carbonate-  
417 bearing rocks inside the Earth (e.g. Liu and Lange 2003). This approach is less straightforward in  
418 multi-component melt (Walker et al. 1988) but has been shown to work for carbonate melt (e.g,  
419 Liu et al. 2007). For BaCO<sub>3</sub>, additional experiments are required to determine the melting curve  
420 between 1 bar and 3 GPa in the piston-cylinder press, in order to test the presence of a local  
421 maximum and resolve its exact location. In particular, the experimental configuration of the ionic  
422 conductivity method needs to be modified for measurements at a few GPa using a piston-  
423 cylinder press. More refractory materials such as Ir are needed to replace the Pt capsule and  
424 electrodes for ionic conductivity measurements on BaCO<sub>3</sub> at pressures below 3 GPa and beyond  
425 11 GPa.

426

## 427 **ACKNOWLEDGEMENTS**

428 (*add after acceptance*)

429

## 430 **REFERENCES CITED**

- 431 Antao, S. M., and Hassan, I. (2007). BaCO<sub>3</sub>: high-temperature crystal structures and the *Pmcn* )  
432 *R3m* phase transition at 811 °C. *Physics and Chemistry of Minerals*, 34(8), 573-580.
- 433 Arapan, S., De Almeida, J. S., and Ahuja, R. (2007). Formation of *sp*<sup>3</sup> hybridized bonds and  
434 stability of CaCO<sub>3</sub> at very high pressure. *Physical Review Letters*, 98(26), 268501.
- 435 Arvanitidis, I., Siche, D., and Seetharaman, S. (1996). A study of the thermal decomposition of  
436 BaCO<sub>3</sub>. *Metallurgical and materials transactions B*, 27(3), 409-416.

#6891 Revision 1 to *American Mineralogist*

- 437 Barium carbonate; MSDS Stock No. 10645 [Online]; Alfa Aesar, Thermo Fisher Scientific  
438 Chemicals, Inc.: Ward Hill, MA, Apr 26, 2018.  
439 <https://www.alfa.com/en/content/msds/USA/10645.pdf> (accessed June 2, 2018).
- 440 Bayarjargal, L., Fruhner, C. J., Schrodtr, N., and Winkler, B. (2018). CaCO<sub>3</sub> phase diagram  
441 studied with Raman spectroscopy at pressures up to 50 GPa and high temperatures and  
442 DFT modeling. *Physics of the Earth and Planetary Interiors*, 281, 31-45.
- 443 Boulard, E., Pan, D., Galli, G., Liu, Z., and Mao, W. L. (2015). Tetrahedrally coordinated  
444 carbonates in Earth's lower mantle. *Nature Communications*, 6, 6311.
- 445 Chaney, J., Santillán, J. D., Knittle, E., and Williams, Q. (2015). A high-pressure infrared and  
446 Raman spectroscopic study of BaCO<sub>3</sub>: the aragonite, trigonal and Pmmn  
447 structures. *Physics and Chemistry of Minerals*, 42(1), 83-93.
- 448 Dasgupta, R. (2013). Ingassing, storage, and outgassing of terrestrial carbon through geologic  
449 time. *Reviews in Mineralogy and Geochemistry*, 75(1), 183-229.
- 450 Errandonea, D. (2013). High-pressure melting curves of the transition metals Cu, Ni, Pd, and  
451 Pt. *Physical Review B*, 87(5), 054108.
- 452 Errandonea, D., Somayazulu, M., Häusermann, D., and Mao, H. K. (2003). Melting of tantalum  
453 at high pressure determined by angle dispersive x-ray diffraction in a double-sided laser-  
454 heated diamond-anvil cell. *Journal of Physics: Condensed Matter*, 15(45), 7635.
- 455 Fiquet, G., Guyot, F., Kunz, M., Matas, J., Andrault, D., and Hanfland, M. (2002). Structural  
456 refinements of magnesite at very high pressure. *American Mineralogist*, 87(8-9), 1261-  
457 1265.
- 458 Galiński, M., Lewandowski, A., and Stępniański, I. (2006). Ionic liquids as  
459 electrolytes. *Electrochimica acta*, 51(26), 5567-5580.
- 460 Galwey, A. K., and Brown, M. E. (1999). *Thermal decomposition of ionic solids: chemical*  
461 *properties and reactivities of ionic crystalline phases* (Vol. 86). Elsevier.
- 462 Ghiorso, M. S. (2004). An equation of state for silicate melts. I. Formulation of a general  
463 model. *American Journal of Science*, 304(8-9), 637-678.
- 464 Hayes, W., and Hutchings, M. T. (1989). Ionic Disorder in Crystals at High Temperatures with  
465 Emphasis on Fulorites. In *Ionic Solids at High Temperatures* (pp. 247-362).
- 466 Hazen, R. M., Downs, R. T., and Prewitt, C. T. (2000). Principles of comparative crystal  
467 chemistry. *Reviews in mineralogy and geochemistry*, 41(1), 1-33.

#6891 Revision 1 to *American Mineralogist*

- 468 Herzberg, C., Asimow, P. D., Arndt, N., Niu, Y., Lesher, C. M., Fitton, J. G., Cheadle, M.J. and  
469 Saunders, A. D. (2007). Temperatures in ambient mantle and plumes: Constraints from  
470 basalts, picrites, and komatiites. *Geochemistry, Geophysics, Geosystems*, 8(2).
- 471 Holl, C. M., Smyth, J. R., Laustsen, H. M. S., Jacobsen, S. D., and Downs, R. T. (2000).  
472 Compression of witherite to 8 GPa and the crystal structure of BaCO<sub>3</sub> II. *Physics and*  
473 *Chemistry of Minerals*, 27(7), 467-473.
- 474 Hurt, S. M., and Wolf, A. S. (2018). Thermodynamic properties of CaCO<sub>3</sub>-SrCO<sub>3</sub>-BaCO<sub>3</sub>  
475 liquids: a molecular dynamics study using new empirical atomic potentials for alkaline  
476 earth carbonates. *Physics and Chemistry of Minerals*, 1-16.
- 477 Irving, A. J., & Wyllie, P. J. (1973). Melting relationships in CaO-CO<sub>2</sub> and MgO-CO<sub>2</sub> to 36  
478 kilobars with comments on CO<sub>2</sub> in the mantle. *Earth and Planetary Science Letters*, 20(2),  
479 220-225.
- 480 Isshiki, M., Irifune, T., Hirose, K., Ono, S., Ohishi, Y., Watanuki, T., Nishibori, E., Takata, M.,  
481 and Sakata, M. (2004). Stability of magnesite and its high-pressure form in the lowermost  
482 mantle. *Nature*, 427(6969), 60-63.
- 483 Jones, A. P., Genge, M., and Carmody, L. (2013). Carbonate melts and carbonatites. *Reviews in*  
484 *Mineralogy and Geochemistry*, 75(1), 289-322.
- 485 Judd, M. D., and Pope, M. I. (1972). Energy of activation for the decomposition of the alkaline-  
486 earth carbonates from thermogravimetric data. *Journal of thermal analysis*, 4(1), 31-38.
- 487 Kaminsky, F., Wirth, R., Matsyuk, S., Schreiber, A., and Thomas, R. (2009). Nyerereite and  
488 nahcolite inclusions in diamond: evidence for lower-mantle carbonatitic magmas.  
489 *Mineralogical Magazine*, 73(5), 797-816.
- 490 Katsura, T., and Ito, E. (1990). Melting and subsolidus phase relations in the MgSiO<sub>3</sub>-MgCO<sub>3</sub>  
491 system at high pressures: implications to evolution of the Earth's atmosphere. *Earth and*  
492 *Planetary Science Letters*, 99(1-2), 110-117.
- 493 Kavner, A., and Jeanloz, R. (1998). High-pressure melting curve of platinum. *Journal of applied*  
494 *physics*, 83(12), 7553-7559.
- 495 Kechin, V. V. (2001). Melting curve equations at high pressure. *Physical Review B*, 65(5),  
496 052102.

- 497 L'vov, B. V., and Novichikhin, A. V. (1997). Quantitative interpretation of the evaporation  
498 coefficients for the decomposition or sublimation of some substances in  
499 vacuo. *Thermochimica acta*, 290(2), 239-251.
- 500 Lander, J. J. (1949). Polymorphism and anion rotational disorder in the alkaline earth  
501 carbonates. *The Journal of Chemical Physics*, 17(10), 892-901.
- 502 Leinenweber, K. D., Tyburczy, J. A., Sharp, T. G., Soignard, E., Diedrich, T., Petuskey, W. B.,  
503 Wang, Y., and Mosenfelder, J. L. (2012). Cell assemblies for reproducible multi-anvil  
504 experiments (the COMPRES assemblies). *American Mineralogist*, 97(2-3), 353-368.
- 505 Li, J., Hadidiacos, C., Mao, H. K., Fei, Y., and Hemley, R. J. (2003). Behavior of thermocouples  
506 under high pressure in a multi-anvil apparatus. *High pressure research*, 23(4), 389-401.
- 507 Li, Z., and Li, J. (2015). Melting curve of NaCl to 20 GPa from electrical measurements of  
508 capacitive current. *American Mineralogist*, 100(8-9), 1892-1898.
- 509 Li, Z., Li, J., Lange, R., Liu, J., and Militzer, B. (2017). Determination of calcium carbonate and  
510 sodium carbonate melting curves up to Earth's transition zone pressures with implications  
511 for the deep carbon cycle. *Earth and Planetary Science Letters*, 457, 395-402.
- 512 Lin, C. C., and Liu, L. G. (1997). High-pressure Raman spectroscopic study of post-aragonite  
513 phase transition in witherite (BaCO<sub>3</sub>). *European Journal of Mineralogy*, 785-792.
- 514 Litasov, K. D., Fei, Y., Ohtani, E., Kuribayashi, T., and Funakoshi, K. (2008). Thermal equation  
515 of state of magnesite to 32GPa and 2073K. *Physics of the Earth and Planetary*  
516 *Interiors*, 168(3), 191-203.
- 517 Liu, Q., and Lange, R. A. (2003). New density measurements on carbonate liquids and the partial  
518 molar volume of the CaCO<sub>3</sub> component. *Contributions to Mineralogy and Petrology*,  
519 146(3), 370-381.
- 520 Liu, Q., Tenner, T. J., and Lange, R. A. (2007). Do carbonate liquids become denser than silicate  
521 liquids at pressure? Constraints from the fusion curve of K<sub>2</sub>CO<sub>3</sub> to 3.2 GPa. *Contributions*  
522 *to Mineralogy and Petrology*, 153(1), 55-66.
- 523 Meng, Y., Hrubiak, R., Rod, E., Boehler, R., and Shen, G. (2015). New developments in laser-  
524 heated diamond anvil cell with *in situ* synchrotron x-ray diffraction at High Pressure  
525 Collaborative Access Team. *Review of Scientific Instruments*, 86(7), 072201.

#6891 Revision 1 to *American Mineralogist*

- 526 Müller, J., Koch-Müller, M., Rhede, D., Wilke, F. D., and Wirth, R. (2017). Melting relations in  
527 the system  $\text{CaCO}_3\text{-MgCO}_3$  at 6 GPa. *American Mineralogist: Journal of Earth and*  
528 *Planetary Materials*, 102(12), 2440-2449.
- 529 Nie, S., Liu, Y., Liu, Q., Wang, M., and Wang, H. (2017). Phase transitions and thermal  
530 expansion of  $\text{BaCO}_3$  and  $\text{SrCO}_3$  up to 1413 K. *European Journal of Mineralogy*, 29(3),  
531 433-443.
- 532 Ono, S. (2007). New high-pressure phases in  $\text{BaCO}_3$ . *Physics and Chemistry of Minerals*, 34(4),  
533 215-221.
- 534 Ono, S., Brodholt, J. P., and Price, G. D. (2008). Phase transitions of  $\text{BaCO}_3$  at high pressures.  
535 *Mineralogical Magazine*, 72(2), 659-665.
- 536 Prescher, C., and Prakapenka, V. B. (2015). DIOPTAS: a program for reduction of two-  
537 dimensional X-ray diffraction data and data exploration. *High Pressure Research*, 35(3),  
538 223-230.
- 539 Prewitt, C. T., and Downs, R. T. (1998). High-pressure crystal chemistry. *Reviews in*  
540 *mineralogy*, 37, 284-318.
- 541 Putirka, K. D., Perfit, M., Ryerson, F. J., and Jackson, M. G. (2007). Ambient and excess mantle  
542 temperatures, olivine thermometry, and active vs. passive upwelling. *Chemical Geology*,  
543 241(3-4), 177-206.
- 544 Rapoport, E., and Pistorius, C. W. (1967). Orthorhombic/disordered rhombohedral transition in  
545  $\text{SrCO}_3$  and  $\text{BaCO}_3$  to 40 kilobars. *Journal of Geophysical Research*, 72(24), 6353-6357.
- 546 Redfern, S. A. (2000). Structural variations in carbonates. *Reviews in Mineralogy and*  
547 *Geochemistry*, 41(1), 289-308.
- 548 Rumble, J. R. (Ed.). (2018). *CRC Handbook of Chemistry and Physics, 98th Edition* (Internet  
549 Version 2018), CRC Press/Taylor and Francis.
- 550 Shatskiy, A. F., Litasov, K. D., and Palyanov, Y. N. (2015). Phase relations in carbonate systems  
551 at pressures and temperatures of lithospheric mantle: review of experimental data. *Russian*  
552 *Geology and Geophysics*, 56(1-2), 113-142.
- 553 Seto, Y., Nishio-Hamane, D., Nagai, T., and Sata, N. (2010). Development of a software suite on  
554 X-ray diffraction experiments. *Review of High Pressure Science and Technology*, 20(3).

#6891 Revision 1 to *American Mineralogist*

- 555 Solopova, N. A., Dubrovinsky, L., Spivak, A. V., Litvin, Y. A., and Dubrovinskaia, N. (2015).  
556 Melting and decomposition of MgCO<sub>3</sub> at pressures up to 84 GPa. *Physics and Chemistry of*  
557 *Minerals*, 42(1), 73-81.
- 558 Stern, K. H. and Weise, E. L. (Ed.). (1969) High temperature properties and decomposition of  
559 inorganic salts, Part II: Carbonates. *National Standard Reference Data System, National*  
560 *Bureau of Standards*, 30, 12-13.
- 561 Stixrude, L., and Karki, B. (2005). Structure and freezing of MgSiO<sub>3</sub> liquid in Earth's lower  
562 mantle. *Science*, 310(5746), 297-299.
- 563 Thomson, A. R., Walter, M. J., Kohn, S. C., and Brooker, R. A. (2016). Slab melting as a barrier  
564 to deep carbon subduction. *Nature*, 529(7584), 76-79.
- 565 Townsend, J. P., Chang, Y. Y., Lou, X., Merino, M., Kirklin, S. J., Doak, J. W., Issa, A.,  
566 Wolverton, C., Tkachev, S.N., Dera, P., and Jacobsen, S. D. (2013). Stability and equation  
567 of state of post-aragonite BaCO<sub>3</sub>. *Physics and Chemistry of Minerals*, 40(5), 447-453.
- 568 Walker, D., Agee, C. B., and Zhang, Y. (1988). Fusion curve slope and crystal/liquid buoyancy.  
569 *Journal of Geophysical Research: Solid Earth*, 93(B1), 313-323.
- 570 Wang, M., Liu, Q., Nie, S., Li, B., Wu, Y., Gao, J., Wei, X. and Wu, X. (2015). High-pressure  
571 phase transitions and compressibilities of aragonite-structure carbonates: SrCO<sub>3</sub> and  
572 BaCO<sub>3</sub>. *Physics and Chemistry of Minerals*, 42(6), 517-527.
- 573 Wu, T. C., Shen, A. H., Weathers, M. S., Bassett, W. A., and Chou, I. M. (1995). Anisotropic  
574 thermal expansion of calcite at high pressures: An *in situ* X-ray diffraction study in a  
575 hydrothermal diamond-anvil cell. *American Mineralogist*, 80(9-10), 941-946.
- 576 Zaoui, A., and Shahrour, I. (2010). Molecular dynamics study of high-pressure polymorphs of  
577 BaCO<sub>3</sub>. *Philosophical Magazine Letters*, 90(9), 689-697.